doi:10.1016/j.jmb.2012.01.058 J. Mol. Biol. (2012) 417, 440–453

Contents lists available at www.sciencedirect.com

Journal of Molecular Biology

journal homepage: http://ees.elsevier.com.jmb

The NOXO1β PX Domain Preferentially Targets PtdIns(4,5)P_2 and PtdIns(3,4,5)P_3

Nicole Y. Davis, Linda C. McPhail and David A. Horita*

Department of Biochemistry, Wake Forest School of Medicine, Winston-Salem, NC 27157, USA

Received 5 January 2012;
accepted 30 January 2012
Available online
8 February 2012

Edited by M. F. Summers

Keywords:
NMR spectroscopy;
reactive oxygen species;
Nox1;
protein–lipid interactions;
phosphatidylinositol

NOXO1β [NOXO1 (*Nox* organizer *1*) β] is a cytosolic protein that, in conjunction with NOXA1 (*Nox* activator *1*), regulates generation of reactive oxygen species by the NADPH oxidase 1 (Nox1) enzyme complex. NOXO1β is targeted to membranes through an N-terminal PX (*phox* homology) domain. We have used NMR spectroscopy to solve the structure of the NOXO1β PX domain and surface plasmon resonance (SPR) to assess phospholipid specificity. The solution structure of the NOXO1β PX domain shows greatest similarity to that of the phosphatidylinositol 3-kinase-C2α PX domain with regard to the positions and types of residues that are predicted to interact with phosphatidylinositol phosphate (PtdInsP) head groups. SPR experiments identify PtdIns(4,5)P_2 and PtdIns(3,4,5)P_3 as preferred targets of NOXO1β PX. These findings contrast with previous lipid overlay experiments showing strongest binding to monophosphorylated PtdInsP and phosphatidylserine. Our data suggest that localized membrane accumulation of PtdIns(4,5)P_2 or PtdIns(3,4,5)P_2 may serve to recruit NOXO1β and activate Nox1.

Introduction

Reactive oxygen species (ROS) generated by NADPH oxidase 1 (Nox1) are involved in cell death/survival,[1] tumor angiogenesis,[2] and motility/invasiveness.[3] Nox1 is a member of the NOX/DUOX family of oxidases, integral membrane proteins with the ability to catalyze transfer of electrons from NADPH to O_2 with formation of superoxide. Full activation involves association of the membrane-integral Nox1/p22^{phox} heterodimer with cytosolic proteins Rac1, NOXO1 (*Nox* organizer *1*), and NOXA1 (*Nox* activator *1*). Association of NOXA1 with Nox1 is likely the principal activating step, but NOXA1 has low intrinsic affinity for Nox1 and no membrane-targeting properties. Rather, NOXA1 is stabilized at the oxidase through association with Rac1, which targets membranes via C-terminal prenyl-/geranylgeranylation and poly-basic motifs, and NOXO1, which targets p22^{phox} via tandem SH3 domains and targets membranes via an N-terminal PX (*phox* homology) domain.[4,5] The activated complex is thus similar to the activated phagocytic oxidase complex, which includes association of membrane-integral NADPH oxidase 2 and p22^{phox} with cytosolic proteins p47^{phox} (a NOXO1 homolog), p67^{phox} (a NOXA1 homolog), p40^{phox}, and Rac.

NOXO1 exists as four splice variants, α–δ, which differ by insertions/deletions within the PX domain.[6] NOXO1β is the major variant, while NOXO1γ is abundant in testis. PX domains are ~130-residue domains that function in protein or

**Corresponding author.* Department of Biochemistry, Wake Forest School of Medicine, Medical Center Boulevard, Winston-Salem, NC 27157, USA.
E-mail address: dhorita@wakehealth.edu.

Abbreviations used: CISK, cytokine-independent survival kinase; PI3K, phosphatidylinositol 3-kinase; Nox1, NADPH oxidase 1; ROS, reactive oxygen species; SPR, surface plasmon resonance; NOE, nuclear Overhauser enhancement; PC, phosphatidylcholine; PE, phosphatidylethanolamine; HSQC, heteronuclear single quantum coherence; CIL, Cambridge Isotope Laboratories, Inc.; COSY, correlated spectroscopy; NOESY, NOE spectroscopy.

phospholipid targeting. Structures of the p40^{phox} and Grd19p PX domains bound to short acyl chain PtdIns(3)P identify a consensus PtdIns-binding pocket and show an Arg residue coordinating the D3 phosphate.[7,8] Similar pockets are present in all structures of PtdIns-binding PX domains. Variations in the size of the pocket and in the identity of residues that contact the PtdIns head group appear to dictate specificity of a given PX domain for a given phosphorylated PtdIns. Protein–lipid overlay analyses of NOXO1β suggest a broad preference for anionic phosphatidylinositols, including PtdIns(3,5)P_2, PtdIns(3)P, PtdIns(4)P, and PtdIns(5)P. Cell localization studies show that NOXO1β is constitutively membrane bound and that this localization is dependent on the PX domain.[9–11] The constitutive membrane localization, and hence activation of Nox1, by NOXO1β is consistent with constitutive ROS production observed in HEK293 cells transfected with murine Nox1, NOXA1, and NOXO1.[12] In contrast, the p47^{phox} PX domain shows preference for PtdIns(3,4)P_2, which is generated by phosphatidylinositol 3-kinase (PI3K) in stimulated cells;[13] phagocytic NADPH oxidase 2, which is regulated in part by colocalization with p47^{phox}, is not active in unstimulated macrophages or neutrophils. Notably, studies in which human (rather than murine) Nox1, NOXA1, and NOXO1 genes are transfected show weak basal ROS generation, with phorbol ester stimulus required for maximal activity,[9,14,15] indicating the existence of a stimulus-dependent activation mechanism.

To address the question of whether the NOXO1β PX domain can target the plasma membrane in a specific phosphatidylinositol-phosphate-dependent manner, we have determined the solution structure of the NOXO1β PX domain using NMR spectroscopy and reevaluated lipid-binding specificity using surface plasmon resonance (SPR). While protein–lipid overlay studies show that the NOXO1β PX domain binds to numerous phosphorylated PtdIns species, a sequence alignment of NOXO1β against other PX domains shows that the residue predicted to interact with the D3 position of the PtdIns ring is Ser, rather than Arg, suggesting that D3-phosphorylated PtdIns should not be a favorable ligand for NOXO1β. The structure of the NOXO1β PX domain described herein shows that the positions of potentially phosphate coordinating Arg residues are most similar to those of the PI3K-C2α PX domain, which shows specificity for PtdIns(4,5)P_2. In contrast to overlay experiments, SPR experiments identify selectivity of the NOXO1β PX domain for PtdIns(4,5)P_2 and PtdIns(3,4,5)P_3, and NMR-detected titration experiments show a structurally specific interaction of NOXO1β PX with PtdIns(4,5)P_2. Localized increases and decreases in PtdIns(4,5)P_2 concentration occur in a variety of cellular processes, including actin-mediated remodeling. Targeting by NOXO1β to localized pools of PtdIns(4,5)P_2 could thus mediate Nox1 activity in a PtdIns-phosphate-dependent manner.

Results

Insights into phospholipid specificity derived from the solution structure and fast timescale dynamics of the NOXO1β PX

We have solved the solution structure of the NOXO1β PX domain using NMR methods with the goal of using this structure to better understand the structural basis of PtdInsP specificity among PX domains. The resultant structures are shown in Fig. 1a and b, while structural statistics are shown in Table 1. Backbone (heavy) atom RMSD over structured regions is 1.03 (2.05) Å. The comparatively high RMSD is a consequence of the need for perdeuteration during resonance assignment and the associated paucity of nuclear Overhauser enhancements (NOEs) among non-exchangeable protons. Inclusion of NOEs from Ile$^{\delta 1}$, Leu, and Val methyl groups and Phe ring protons was critical to convergence. The structures satisfy NMR restraints, Ramachandran backbone, and Whatcheck packing criteria.

The growing body of PX domain structures yields a set of structure-based predictive rules for PtdIns-phosphate-binding specificity. The crystal structure of the p40^{phox} PX domain bound to PtdIns(3)P shows coordination of the D3 phosphate by R58.[7] p47^{phox}[16] contains the structurally analogous R43, which presumably coordinates the D3 phosphate in the p47^{phox} PX target PtdIns(3,4)P_2. R50 in the cytokine-independent survival kinase (CISK) PX domain, which binds PtdIns(3,4,5)P_3, PtdIns(3,5)P_2, and, to a lesser degree, PtdIns(4,5)P_2,[17] is likewise positioned to coordinate a D3 phosphate.[18] [The CISK PX has also been described as PtdIns(3)P specific.[19]] Thus, a positively charged residue in this position is strongly conserved among PX domains that have high affinity for D3-phosphorylated PtdInsP's. In contrast, a hydrogen bond acceptor/donor residue is typically found in PX domains that target non-D3-phosphorylated PtdIns head groups, for example, T1462 in the PI3K-C2α PX domain and Y317 in the Bem1p PX domain, which target PtdIns(4,5)P_2, and PtdIns(4)P, respectively.

Our structure shows that the NOXO1β PX domain has a Ser at the D3-interacting position, suggesting that PtdIns(3)P is not a primary target. Inspection of residues surrounding the PtdInsP-binding pocket shows that the NOXO1β PX domain shows greatest similarity to the PI3K-C2α PX domain,[20,21] which specifically binds PtdIns(4,5)P_2. Compared across 80 C^{α} atoms in secondary structure elements, NOXO1β PX exhibits a 1.49-Å RMSD *versus*

PI3K-C2α PX (2REA) and a 1.88-Å RMSD *versus* p47^{phox} PX (1KQ6). Figure 2 compares PtdInsP-binding-site residues of the PX domains of NOXO1β with p40^{phox} [which binds to PtdIns(3)P], p47^{phox} [PtdIns(3,4)P_2], Bem1p [PtdIns(4)P], CISK [PtdIns(3,4,5)P_3 and PtdIns(3,5)P_2], and PI3K-C2α [PtdIns(4,5)P_2] and shows the presence of an Arg positioned to coordinate a D3 phosphate in p40^{phox}, p47^{phox}, and CISK but the absence of a corresponding Arg in the PI3K-C2α, Bem1p, and NOXO1βPX domains. In all cases, the residue expected to interact with the D4 position is an Arg. An Arg at this position is highly conserved throughout PX domains whether they bind to D4-phosphorylated PtdIns and is not in itself diagnostic of PtdInsP specificity. Instead, factors that appear to contribute to selection for/against D4 and D5 phosphates are the Arg content and the size and conformational flexibility of the binding pocket and the loop immediately preceding helix α_2.

NOXO1β has a relatively open PtdInsP-binding pocket in that α_2 loop—residues do not block access. Analysis of fast timescale dynamics based on ^{15}N relaxation also shows that this loop is disordered. Figure 3 shows results of Modelfree v4.20 analysis ^{15}N T_1, T_2, and NOE measurements and identify a clustering of residues exhibiting nanosecond-scale flexibility (as manifested in elevated τ_e values) in the loop immediately preceding α_2. This section spans the Arg residues (81 and 84) potentially involved in coordination of a D5 phosphate, and the conformation of this loop as depicted in Fig. 2f is one of a structurally diverse ensemble (Fig. 1a, arrow). Notably, the corresponding loop is also disordered in the crystal structures of the PI3K-C2α PX domain, which binds PtdIns(4,5)P_2. Whether disorder in this loop is a requisite for binding to PtdIns(4,5)P_2 or simply a consequence of the longer loop found in these two PX domains will require further analysis and, preferably, a structure of a PX domain bound to a lipid other than PtdIns(3)P. Most other regions in NOXO1β with elevated τ_e or R_{ex} are sparsely distributed or of small magnitude, with the notable exception of the loop preceding strand β_4.

Strand β_4, unambiguously identified in our NOXO1β PX structure, runs antiparallel with β_1

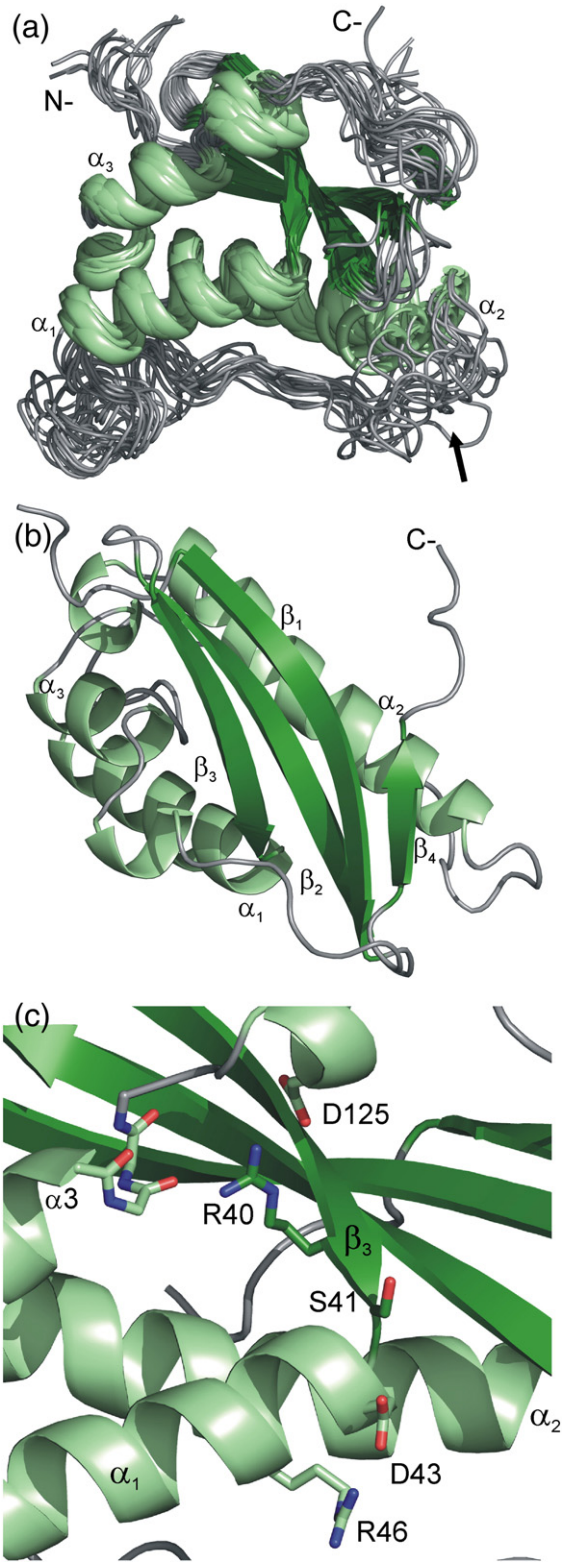

Fig. 1. (a) Overlay of 14 lowest-energy structures of the NOXO1β PX domain. Enhanced τ_e values for the α_1–α_2 loop identify conformational diversity at the PtdInsP-binding pocket (arrow). Helices are colored light green; strands, dark green; and extended/coil, gray. (b) Low-energy structure, rotated 90° on the horizontal axis from (a), with conserved secondary structural elements labeled. The fourth β-strand is common to NOXO1β and p47^{phox}. (c) The R40 guanidino group interacts with the C-terminus of α_3 and the D125 carboxylate. Interaction of the D43 carboxylate with R46 may mitigate electrostatic repulsion at the D3 position of the inositol ring, allowing binding to PtdIns(3,4,5)P_2. Orientation of (c) matches that of (a). Strands are colored dark green; helices, light green; and coil, gray.

Table 1. Refinement statistics for 14 lowest-energy structures of NOXO1β PX

Number of experimental restraints					
Distance restraints from NOEs	Total	Intra	Sequential	Medium	Long
Unambiguous	559	85	155	134	185
Ambiguous	67				
Dihedral					
ϕ ψ	222				
χ_1	97				
Hydrogen bond	63				
RDC	153				
^{1}H shift	53				
RMSD, energy, and average number of violations from experimental restraints					
Restraint	RMSD	Energy (kcal/mol)	Average violations		
NOE distances (Å)	0.15 ± 0.02	162	(>0.5) 4		
Dihedral angles (°)	1.9 ± 0.3	85	(>5) 5		
^{1}H shifts (ppm)	0.09 ± 0.01	22	(>0.2) 2		
RDC (Hz)	0.44 ± 0.04	148			
Q-factor[a]	0.067 ± 0.007				
RMSD from idealized geometry					
Bonds (Å)	0.01 ± 0.00				
Angles (°)	1.3 ± 0.04				
Improper (°)	4.1 ± 0.2				
Total energy (kcal/mol)[b]	−6702				
Coordinate precision	Backbone	Heavy			
Structured[c] (Å)	1.03	2.05			
Ramachandran analysis	m.f.	a.a.	g.a.	dis.	
All	88.1	8.8	1.7	1.4	
Structured[c]	93.4	5.7	0.7	0.3	
Whatcheck *Z*-score					
First-generation packing	−1.96				
Second-generation packing	−2.09				
χ_1/χ_2 normality	−1.23				

[a] Cornilescu *et al*. (1998). *J. Am. Chem. Soc.* **120**, 6836–6837.
[b] Includes all restraints, geometries, and electrostatic energies.
[c] Structured residues span 8–56, 84–120, and 135–138.

(Fig. 1b) and is not a canonical component of PX domains. An analogous strand is found in the X-ray structure of the long construct (1KQ6) of the p47^{phox} PX domain[22] but not in the X-ray (1O7K) or NMR (1GD5) structures of the short construct.[16,23] Across known PX domains, this strand appears to be restricted to the NOXO1/p47^{phox} family, although a C-terminal β-strand antiparallel with β_3 is found in the PX domain of Bem1p.[24] The β_4 strand in p47^{phox} and NOXO1β redirects the C-terminus to point in the other direction and emanates from the opposite side, relative to most known PX domain structures. This strand thus potentially alters positioning of the PX domain relative to the subsequent domains in NOXO1/p47^{phox} as compared to other PX-domain-containing proteins and shows that the α_3–β_4 loop and β_4 strand are structurally conserved components of this family.

Structural impact of the R40Q mutation

The R40Q mutation to the NOXO1β PX domain disrupts lipid binding *in vitro* and membrane localization *in vivo*.[9] This mutation is the analog of

Fig. 2. Comparison of PtdInsP-binding sites for PX domains with specificity for different PtdIns phosphates. View is into the PtdInsP-binding pocket. (a) p40^{phox} (1H6H) bound to PtdIns(3)P; (b) p47^{phox} (1KQ6), which shows preference for PtdIns(3,4)P_2; (c) Bem1p (2CZO), which shows preference for PtdIns(4)P; (d) CISK (1XTE), which shows preference for PtdIns(3,4,5)P_3 and PtdIns(3,5)P_2; (e) PI3K-C2α (2REA), which shows preference for PtdIns(4,5)P_2; (f) NOXO1β, which shows preference for PtdIns(4,5)P_2 and PtdIns(3,4,5)P_3. Helices α_1 and α_2 are labeled for reference. Circled residues are in position to coordinate the D3 phosphate/hydroxyl moiety of the inositol ring. Labeled Arg residues presumably coordinate phosphate/hydroxyl moieties at D4 and D5 (full electron density is missing for PI3K-C2α R1493). (g) Structure-based alignment of PX domains. The end of β_3 and the start of α_2 are marked. The blue box marks the residue that interacts with the D3 position of the PtdIns head group, and the green box marks the residue that interacts with the D4 position (based on the p40^{phox} and Grd19p PX structures). Residues potentially positioned to coordinate a D5 phosphate are shown in red (CISK N81 has been proposed to hydrogen bond to the D5 phosphate). Residues conserved in the α_1–α_2 loops of NOXO1β and PI3K-C2α are shown in boldface. Residues in the loop immediately preceding α_2 are conformationally divergent among solved PX domain structures (black box). NOXO1γ contains a five-residue insertion between NOXO1β L74/D75. Primary PtdInsP specificities for each PX domain are listed on the right.

the R42Q mutation in p47^{phox}, which is found in patients with chronic granulomatous disease[25] and which also disrupts membrane localization *in vivo*.[13] This mutation is frequently used as a negative lipid-binding control for both p47^{phox} and NOXO1β. However, our structure clearly shows that Ser41, and not Arg40, occupies the PtdIns D3 coordination position (Fig. 1c). The side chain of R40/42 is largely buried in both NOXO1β and p47^{phox},[16,22,23] and in both domains, the Arg guanidino group mitigates the negative charges from D125 (NOXO1β)/D124 (p47^{phox}) and the C-cap of helix α_3 and seals the

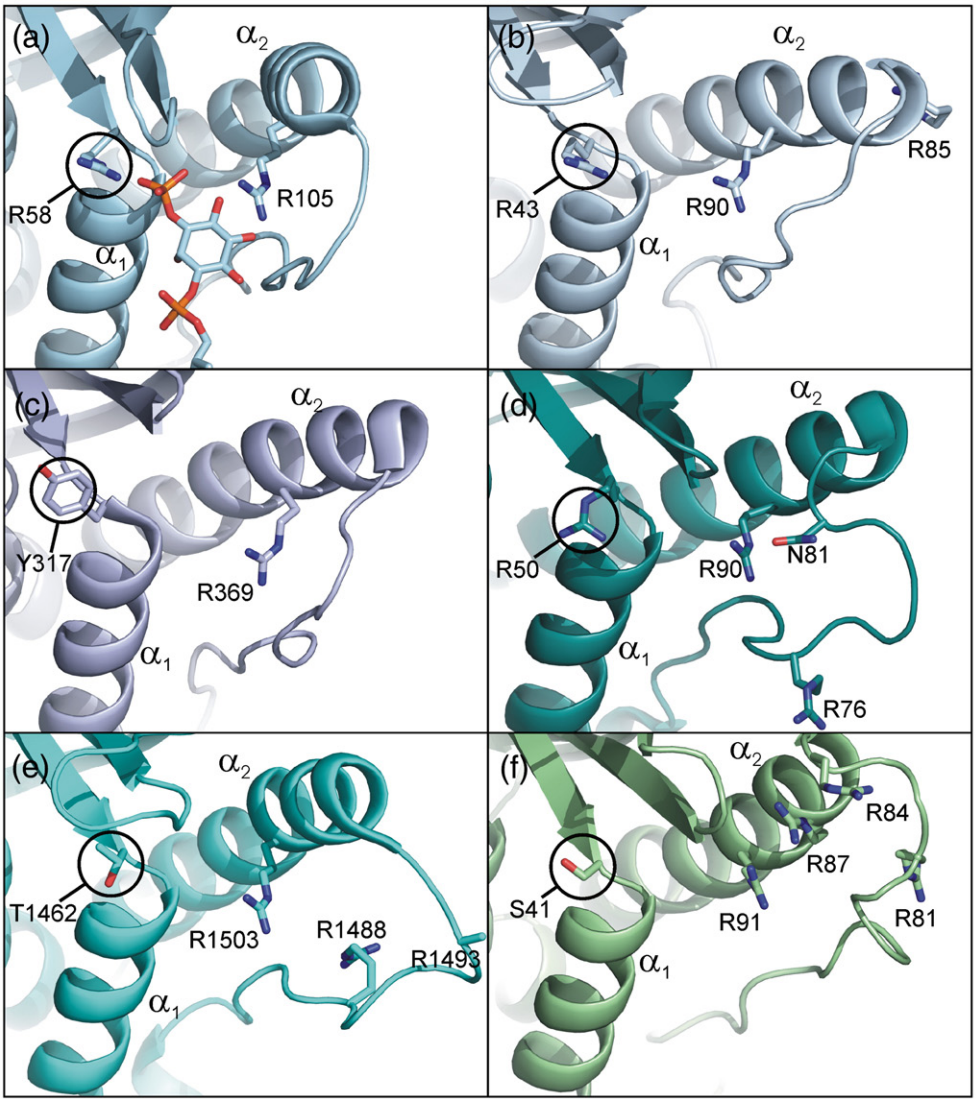

(g)

	β3	α2	
p40^{phox}	^{54}LIYRRYR	^{84}CTLPTLPAKVY VGVKQEIAEMR	PI(3)P
p47^{phox}	^{39}VVYRRFT	^{70}RIIPHLPAPK WFDGQRAAENR	PI(3,4)P_2
Bem1p	^{313}QLKRYYQ	^{349}RIMPYIPGPV PYVTNSITKKR	PI(4)P
CISK	^{46}FVFRRYA	^{67}AMALKIPAKRIFGDNFDPDFIKQR	PI(3,4,5)P_3, PI(3,5)P_2
PI3K-C2α	^{1458}FVFRTFD	^{1480}WKLPGFPNRMV**LGR**THIKDVAAKR	PI(4,5)P_2
NOXO1β	^{37}FVRRSWD	^{68}RVLPKLLDAPL**LGR**VGRTSRGLAR	PI(4,5)P_2, PI(3,4,5)P_3
NOXO1γ		GQASL	

Fig. 2 (*legend on previous page*)

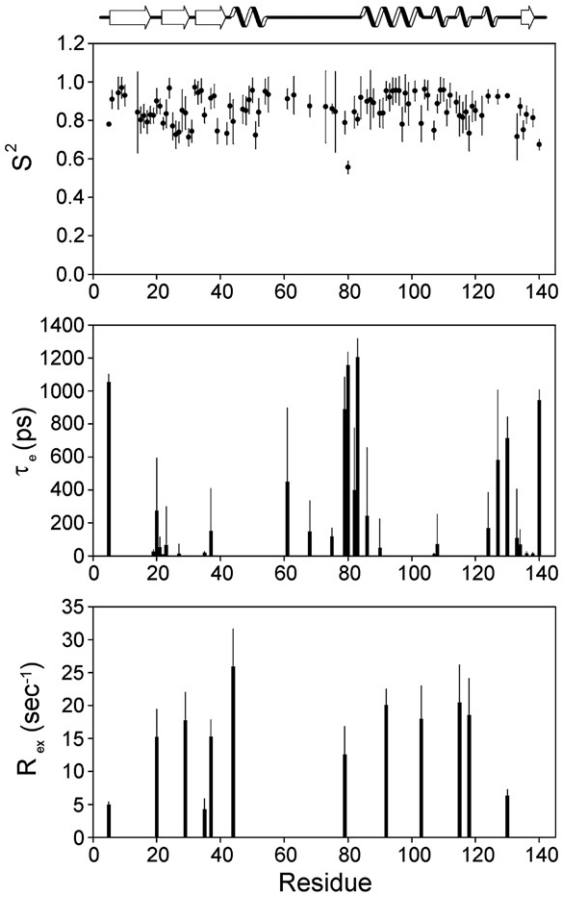

Fig. 3. NOXO1β PX domain backbone dynamics as determined by ^{15}N relaxation. Plotted are best-fit S^2, τ_e, and R_{ex} as calculated by Modelfree 4.20 for motional models determined by FAST-Modelfree. Residues in the loop preceding helix α_2 exhibit elevated values of τ_e.

hydrophobic core from solvent. A Gln side chain lacks the positive charge and is too short to fulfill these interactions. Thus, the R40Q (NOXO1β)/R42Q (p47^{phox}) mutation[9,13] likely disrupts protein–lipid binding by destabilizing the PX domain, rather than abrogating a specific Arg–phosphate interaction, consistent with the findings that this mutation to p47^{phox} in patients with chronic granulomatous disease results in the absence, rather than mislocalization, of p47^{phox}.[26]

Phospholipid-binding specificity of the NOXO1β PX domain

SPR analysis

The notable structural similarity to a PtdIns(4,5)P_2-specific PX domain prompted us to further examine lipid-binding specificity through direct means. We performed SPR experiments in which we flowed NOXO1β PX across a phospholipid surface consisting of a phosphatidylcholine (PC)/phosphatidylethanolamine (PE) bilayer with/without 6 mol% PtdInsP. Figure 4a–c shows sample SPR traces for NOXO1β PX binding to PtdIns(3)P and PtdIns(4,5)P_2 and p40^{phox} PX binding to PtdIns(3)P. The high level of binding to the control surface is NOXO1β specific, as p40^{phox} PX exhibits minimal [0–50 RU (*r*esonance *u*nits)] binding to the reference lane and substantial (several hundred RU) binding to 3 mol% PtdIns(3)P under identical running conditions. We observed reproducible, statistically significant increased binding to PC/PE surfaces containing 6 mol% PtdIns(4,5)P_2 and PtdIns(3,4,5)P_3 at 5 and 10 μM protein concentrations ($p < 0.05$, Dunn's post-hoc analysis). NOXO1β shows no significant binding *versus* background to any of the other PtdInsP's (Fig. 4d and e). Binding to PtdIns(3,4)P_2 approaches, but does not reach, statistical significance.

Because NOXO1β PX associated with the control PC/PE surface at a high level (hundreds of RU for NOXO1β *versus* tens of RU for p40^{phox}), we report our SPR results as ratios, rather than differences, between target and reference lipid lanes. This treatment is necessary because the absolute RU for binding to the control surface is dependent on the amount of lipid deposited on the L1 chip surface, and this is difficult to control the degree necessary to make analysis of RU differences consistent and meaningful over the 10 lipid compositions we tested. ANOVA of the entire data set shows larger between than within group variance, indicating (1) that the use of RU ratios is sufficiently robust to accommodate differences in initial lipid loading and (2) that the NOXO1β PX domain has quantitatively distinct binding preferences for specific PtdInsP's. Post-hoc analysis using Dunn's method identified binding to PtdIns(4,5)P_2 and PtdIns(3,4,5)P_3 as statistically significant. Although the use of RU ratios allows us to extract useful information from our SPR data, it does not allow fitting of association/dissociation curves or selection of a binding model. We also noted frequent clogging of the Biacore flowpath at protein concentration levels sufficient to saturate binding. Hence, we are unable to quantitatively determine K_d, k_{on}, or k_{off} for NOXO1β PX.

NMR titration

Titration of the NOXO1β PX domain with diC$_4$-PtdIns(4,5)P_2 caused titrable, significant (greater than half of line width) chemical shift changes for numerous residues in helix α_1 (W42, D43, Q47, K49–T51, and E54) and residues in the α_1–α_2 loop (D75) and in the α_2 helix (R91, L94, D96, and L103). An expansion of the initial and terminal heteronuclear single quantum coherence (HSQC) spectra in the

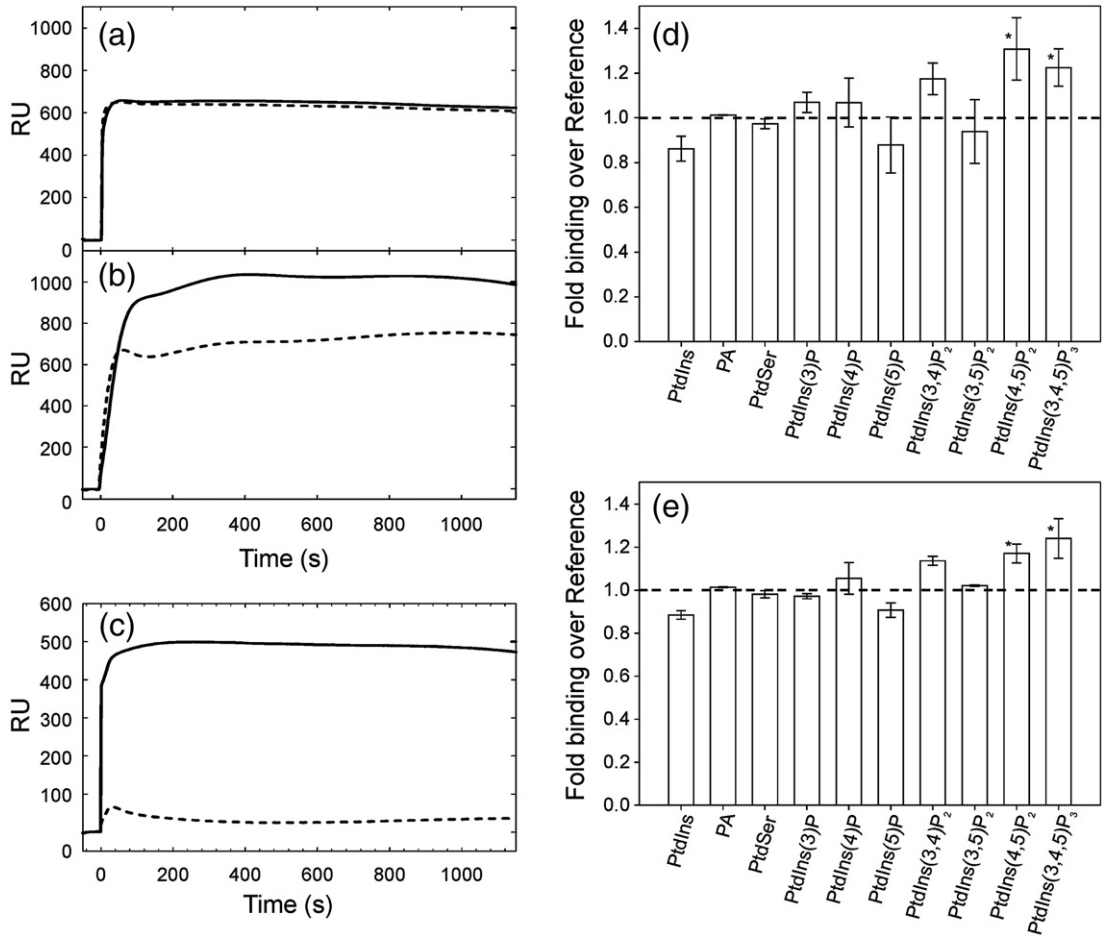

Fig. 4. SPR data for binding by the NOXO1β PX domain to phosphatidylinositols and acidic phospholipids. (a–c) Example SPR traces for 5 μM NOXO1β PX domain binding to 6 mol% (a) PtdIns(3)P and (b) PtdIns(4,5)P_2. (c) Shown is 5 μM $p40^{phox}$ PX domain binding to 3 mol% PtdIns(3)P under the same experimental conditions for comparison. Continuous line shows binding to PtdInsP lane; broken line shows binding to the reference lane. (d and e) Analysis of NOXO1β PX binding to phospholipids in a PE/PC bilayer at (d) 5 μM and (e) 10 μM protein concentrations. Labeled phospholipid was present at 6 mol%. Fold binding over reference is calculated as the ratio of baseline-subtracted target to baseline-subtracted reference lanes. Mean ± SD of binding shows significance ($p < 0.05$) *versus* PtdIns for PtdIns(4,5)P_2 and PtdIns(3,4,5)P_3 using Dunn's post-hoc method following ANOVA.

titration series is shown in Fig. 5a. The residues that exhibit chemical shift changes in the presence of PtdIns(4,5)P_2 cluster on the membrane-binding surface proximal to the putative PtdIns(4,5)P_2-binding pocket (Fig. 5b). In contrast, titration with diC_6-PtdIns(3,4)P_2 did not cause concerted shift changes (Fig. 5c), although some residues appear to have been broadened. These results are consistent with the SPR data in that they identify an interaction between the NOXO1β PX domain and PtdIns(4,5)P_2. Importantly, they differentiate between binding to PtdIns(3,4)P_2 and PtdIns(4,5)P_2. Although we do observe an impact on intensity of several protein residues upon addition of PtdIns(3,4)P_2, this interaction is much weaker and not structurally localized. Given that the NOXO1β PX domain is strongly basic (calculated pI ~11), we suggest that some of the previously observed *in vitro* associations of NOXO1β PX with anionic lipids are driven by nonspecific electrostatic interactions.

Comparison to other NOXO1 isoforms

NOXO1 has four splice variants,[14,15] with differences between proteins contained within the PX domain. NOXO1β is the major isoform. NOXO1α and NOXO1δ lack K50 (NOXO1β numbering), which lies in helix α_1 and is completely surface exposed in our structure. Its absence would alter the helical register, resulting in L52 being surface exposed and K53 being buried, likely disrupting proper folding of the PX domain. Both NOXO1α and NOXO1δ localize to intracellular vesicles and/or form large aggregates when overexpressed,[11]

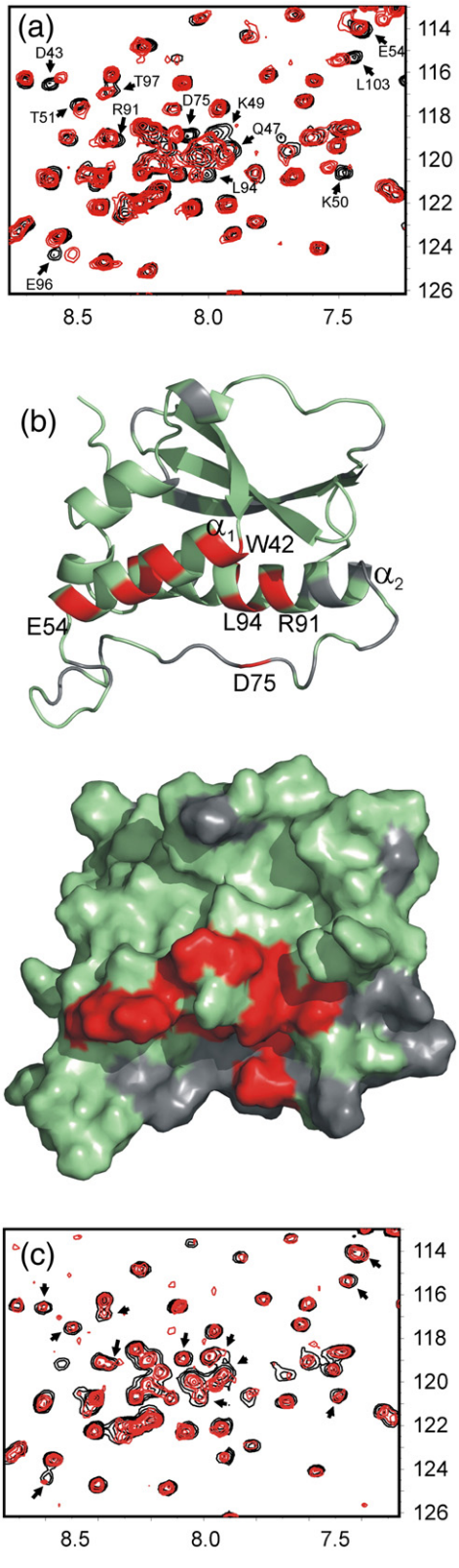

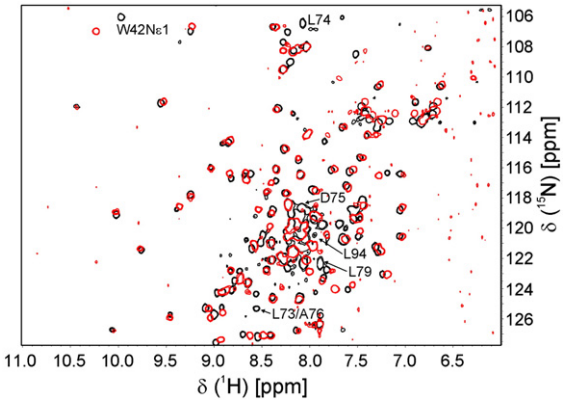

Fig. 6. HSQC spectra of NOXO1β (black) and NOXO1γ (red) PX domains. Overall similarity indicates that both proteins adopt the same fold. Residues that exhibit large shift changes cluster around the insertion point (L74/D75) either in sequence (L73–L79) or space (L94 and W42).

consistent with partial misfolding of the protein. NOXO1γ and NOXO1δ differ from NOXO1β and NOXO1α, respectively, in containing the five-residue insert GQASL between L74 and D75 (NOXO1β numbering). Because this insertion occurs in the long α_1–α_2 loop, it is less likely to disrupt the PX domain structure than the K50 deletion. Indeed, while attempts to purify the NOXO1α PX domain were unsuccessful, we were able to express and purify the NOXO1γ PX domain. Figure 6 shows an overlay of HSQC spectra of the NOXO1β and NOXO1γ PX domains. The similarity of the spectra indicates that both PX domains are folded and that they adopt the same overall fold. The most prominent shift changes occur at the insertion point, spanning L73–A76, and at residues proximal to the insertion point, including L94 in the α_2 helix and the W42 indole. Residues at the position of the Trp often form the back of the PtdIns-binding pocket

Fig. 5. (a) Expansion of NOXO1β PX HSQC spectra in the absence (black) and in the presence (red) of 2-fold molar excess PtdIns(4,5)P_2. Resonances exhibiting significant changes in chemical shift are identified by arrows. (b) Residues matching these resonances are colored red on the NOXO1β PX structure. These residues cluster along helix α_1 and the putative PtdInsP-binding-site residues in the α_1–α_2 loop and helix α_2. The surface representation is in the same orientation as the ribbon diagram and shows clustering of PtdIns(4,5)P_2-interacting residues at the phospholipid-binding pocket. Residues exhibiting no shift changes are green, and missing/overlapped residues are gray. (c) Expansion of HSQC spectra in the absence (black) and in the presence (red) of 2-fold molar excess PtdIns(3,4)P_2. Arrows mark the same residues as in (a). Although several resonances broaden, no residue shows titrable shift changes.

in other PX domain structures. Smaller but concerted shift changes are observed in neighboring residues spanning L70–V82. NOXO1γ exhibits decreased localization to the plasma membrane and is largely localized in the nucleus[11] or cytoplasm.[10] This change in localization could be a direct result of differing PtdInsP specificity or affinity between the isoforms or an indirect result of differing intramolecular or intermolecular interactions between the PX domain and other NOXO1 domains or distinct proteins. Notably, the residues that show shift changes between isoforms are included among those that show shift changes upon addition of PtdIns(4,5)P_2. A more detailed analysis of NOXO1γ will be required to determine the impact of the five-residue insertion on protein structure and lipid binding.

Discussion

We have determined the solution structure of the NOXO1β PX domain and investigated its preferential PtdInsP target using lipid overlay experiments (Supplemental Fig. 1) and SPR- and NMR-based experiments. Our structural data show that both the PtdInsP-binding-pocket size and the presence of localized disorder are similar to those observed for the PtdIns(4,5)P_2-binding PI3K-C2α but distinct from the PtdIns(4)P-binding Bem1p PX domains, which has a smaller and more rigid pocket. Stahelin *et al*. have proposed that the loop immediately preceding helix α_2 establishes a steric barrier against D5-phosphorylated PtdInsP's in Bem1p.[24] This loop is several residues longer in NOXO1β, CISK, and PI3K-C2α than in $p40^{phox}$, $p47^{phox}$, or Bem1p (Fig. 2g). The crystal structures of the PI3K-C2α PX domain are missing electron density for residues in this loop (e.g., no density for residues 1488–1497 in 2IWL and weak side-chain density for residues 1490–1496 in 2REA), suggesting that the PtdIns(4,5)P_2-binding loop is disordered in the unbound state. In contrast, the analogous loop residues in crystal structures of $p40^{phox}$, $p47^{phox}$, and Bem1p are well defined. Additional selectivity for a D5 phosphate presumably arises from the Arg residues present in this loop in PI3K-C2α, CISK, and NOXO1β but absent in Bem1p, $p40^{phox}$, and $p47^{phox}$. Mutation of R1493A in PI3K-C2α causes a 23-fold increase in K_d for PtdIns(4,5)P_2.[21] Notably, this residue is conserved in NOXO1β (R81; Fig. 2g), consistent with coordination of a D5 phosphate. While the PI3K-C2α PX domain is specific for PtdIns(4,5)P_2,[27] our SPR experiments show that NOXO1β is also able to interact with PtdIns(3,4,5)P_3. Both NOXO1β and PI3K-C2α PX domains contain an Asp at the beginning of α_1 (D43 and D1464 in NOXO1β and PI3K-C2α, respectively) that would provide unfavorable electrostatic interactions with the D3 phosphate. However, the negative change could be mitigated in NOXO1β by R46, which is on the same side of α_1 and forms a salt bridge to D43 in our structures (Fig. 1c). The Gln at residue 1467 in PI3K-C2α cannot form a similar interaction.

The differences in PtdInsP-binding specificity observed for the NOXO1β PX domain may result from the different physical presentations of target phospholipids in each of the assays used. Lipid overlays present long-chain PtdInsP's adhered to nitrocellulose membranes, SPR presents long-chain PtdInsP's embedded in a PE/PC bilayer, and NMR presents short-chain PtdInsP in solution. Lipid overlay assays, while convenient, have the potential to generate misleading data, especially with regard to phospholipid specificity of PX domains.[28] Collectively, in our (Supplemental Data) and others' hands,[9–11] the NOXO1β PX domain exhibits binding to PtdIns(3)P, PtdIns(4)P, PtdIns(5)P, and PtdIns(3,5)P_2, as well as phosphatidic acid and phosphatidylserine. Notably, each group has obtained a different subset of binding specificities, highlighting a difficulty in interpreting NOXO1β binding data. SPR analysis, while substantially more time, labor, and equipment intensive than lipid overlay experiments, has been identified as a preferable method of testing phospholipid-binding specificity of proteins.[29] Our SPR analysis reveals a statistically significant increase in binding by the NOXO1β PX domain to PtdIns(4,5)P_2 and PtdIns(3,4,5)P_3 *versus* control (PE/PC or PE/PC/PtdIns). Binding to PtdIns(3,4)P_2 approaches significance, while binding to PtdIns monophosphates is not significant. In comparison, only minimal binding to either PtdIns(4,5)P_2 or PtdIns(3,4,5)P_3 is observed in lipid overlay experiments. Our NMR titration experiments extend our SPR results and further differentiate between site-specific binding to PtdIns(4,5)P_2 *versus* weaker, nonspecific binding to PtdIns(3,4)P_2.

In quiescent cells, PtdIns(4)P and PtdIns(4,5)P_2 each constitute nearly 50% of the phosphorylated PtdIns content, with PtdIns(3)P and PtdIns(5)P constituting ~2% each and PtdIns(3,4)P_2, PtdIns(3,5)P_2, and PtdIns(3,4,5)P_3 constituting ~0.1% each.[30] PtdIns(4,5)P_2 is concentrated in the plasma membrane, PtdIns(4)P is distributed between the plasma membrane and the Golgi, and PtdIns(3)P is largely found in early endosomes.[31,32] Our structure and NMR- and SPR-derived binding data suggest that the previously observed constitutive localization to the membrane by NOXO1β is due to its interaction with PtdIns(4,5)P_2, rather than PtdIns(3)P or PtdIns(4)P as suggested by lipid overlay experiments. As noted by Stahelin *et al*., PX-domain-mediated targeting *in vivo* depends both on the affinity for a particular PtdInsP of the PX domain and on the availability of each PtdInsP species.[33] Given that the NOXO1β PX domain shows particular affinity

to PtdIns(4,5)P_2 as measured by SPR and NMR titration experiments and that this phospholipid is by far the predominant PtdInsP in resting cell plasma membranes, we suggest that PtdIns(4,5)P_2 is the primary lipid target of NOXO1β.

Nox1-generated ROS are involved in numerous cellular processes involving cytoskeletal remodeling and cell migration.[34–36] Notably, localized accumulation of PtdIns(4,5)P_2 is associated with recruitment of actin-modifying proteins and actin polymerization, a hallmark of cell migration and cytokinesis.[37] Thus, while PtdIns(4,5)P_2 is distributed throughout the plasma membrane in quiescent cells, variation in localized concentration is observed in multiple cellular processes. Our finding that NOXO1β targets PtdIns(4,5)P_2 thus provides a possible link between accumulation at sites of cytoskeletal remodeling of PtdIns(4,5)P_2 and the spatially and temporally localized activation of Nox1. The ability of NOXO1β to bind to PtdIns(3,4,5)P_3 also suggests that phosphorylation at D3 of PtdIns(4,5)P_2 will not abrogate targeting by NOXO1β and thus not inhibit ROS production by Nox1. Overall, our structure and SPR and NMR titration analyses of the NOXO1β PX domain suggest a primary *in vivo* target of PtdIns(4,5)P_2. However, prediction of PtdIns specificity based on PX domain structure remains challenging, likely due to observed flexibility at the ligand-binding pocket and conformational changes at the pocket upon ligand binding.

Materials and Methods

Protein expression and purification

The human NOXO1β PX domain (residues 1–144) was isolated by PCR from the full-length clone (gift of Tom Leto), inserted into pGEX-6P1, and expressed as a GST (*g*lutathione *S*-*t*ransferase)-fusion protein in BL21(DE3) CodonPlus RIPL cells (Stratagene) and purified as previously described.[38] Optimal expression of soluble protein was achieved at 32 °C. Later experiments used a pET47b-based plasmid into which maltose-binding protein had been inserted and the protease cleavage site had been modified to match that of pGEX-6P1. This plasmid gave substantially higher expression levels (10 mg final product per liter of culture). Purification followed that of the GST-fusion with the addition of a Ni-NTA (Qiagen) column step for initial capture and elimination of the glutathione-Sepharose column step. The plasmid coding for the NOXO1γ PX domain was constructed by mutagenesis of the NOXO1β/pGEX-6P1 construct using the QuikChange protocol (Stratagene). NOXO1γ PX expression (^{15}N) and purification followed that of NOXO1β PX.

All proteins were expressed in M9 minimal media, and all proteins were cleaved from their fusion partners using Prescission Protease (GE Biosciences). Protein samples for SPR were dialyzed into 20 mM Hepes (pH 7.1), 137 mM KCl, 1 mM $MgCl_2$, and 1 mM ethylene glycol bis(β-aminoethyl ether) *N*,*N*′-tetraacetic acid (SPR buffer). Perdeuterated samples were grown in >99% D_2O (Spectra Stable Isotopes) with $^{15}NH_4Cl$ [Sigma-Isotec and Cambridge Isotope Laboratories, Inc. (CIL)] and $^{2}H_7^{13}C_6$-glucose (CIL) as sole nitrogen and carbon sources. I(δ_1) LV-methyl protonated samples were produced by addition of 100 mg 2-keto-3-(methyl-d_3)-butyric acid and 50 mg 2-ketobutyric acid ($^{13}C_4$, 3,3-d_2) (CIL and Sigma-Isotec) prior to induction. I(δ_1)LV-methyl, $^{1}H/^{12}C/^{15}N$–F samples were produced by addition of 100 mg 2-keto-3-(methyl-d_3)-butyric acid, 50 mg 2-ketobutyric acid ($^{13}C_4$, 3,3-d_2), and 40 mg ^{15}N phenylalanine (CIL) prior to induction.

The p40^{phox} PX domain (residues 2–149) was cloned into pET49b (EMD) as a GST-His_6-fusion and expressed in BL21(DE3) CodonPlus RIPL cells (Stratagene) overnight at 15 °C. Fusion protein was captured by application to glutathione-Sepharose FF resin (GE Biosciences). The fusion protein was eluted from the column, cleaved from the GST tag overnight using Prescission Protease, purified by sequential application to glutathione-Sepharose FF and SourceQ columns (GE Biosciences), and dialyzed into SPR buffer.

NMR data acquisition

NMR spectra were acquired at 293 K on a Bruker Avance DRX-600 spectrometer equipped with a triple-resonance Z-gradient cryoprobe. Samples were dialyzed into 100 mM NaP_i, 100 mM NaCl, and 0.1 mM ethylenediaminetetraacetic acid (pH 6.5). Five percent (v/v) $^{2}H_5$ glycerol was added after samples were concentrated. NOXO1β and NOXO1γ PX domains were concentrated to ~500 μM for all NMR experiments except as otherwise noted. The use of a 4-mm Shigemi sample tube inserted into a 5-mm flat-bottom tube containing D_2O provided 30% shorter ^{1}H pulses (*versus* a 5-mm sample tube), allowed use of 100% H_2O for the sample buffer, and afforded equivalent signal/noise as a same-concentration sample in a 5-mm NMR tube. As previously noted,[38] perdeuteration of the protein was necessary to observe magnetization transfer among side-chain carbons. Analysis of the ^{15}N relaxation experiments yielded a rotational correlation time of 14.6 ns. Size-exclusion chromatography was consistent with a monomeric protein, and we noticed no concentration-dependent changes in chemical shifts between 50 μM and 1 mM. The long correlation time is a consequence of temperature (293 K) and inclusion of glycerol, both of which extended protein stability. For PtdInsP titration experiments, $^{2}H/^{15}N$-labeled protein (80 μM) was dialyzed into 20 mM Hepes (pH 7.2), 137 mM KCl, and 0.1 mM ethylene glycol bis(β-aminoethyl ether) *N*,*N*′-tetraacetic acid. diC_6-PtdIns(3,4)P_2 (Cayman Chemical, Ann Arbor, MI) or diC_4-PtdIns(4,5)P_2 (Echelon Biosciences, Inc., Salt Lake City, UT) was dissolved in titration buffer at 160 μM and added to the protein solution to give protein: lipid ratios of 1:0, 0.25, 0.5, 0.75, 1, and 2.

Resonance assignment

H^N, N, C, C^α, and C^β shifts were assigned as described previously.[38] Methyl groups were assigned using the $H^{me}C^{me}CGCBCA$ sequence,[39] an $H^{me}C^{me}CBCA$ sequence that provided higher sensitivity for Val residues and was

derived from the previous sequence by deleting one carbon transfer step, and the H(C)C(CO)NH/(H)CC(CO)NH total correlated spectroscopy (TOCSY) sequences.[40] We were able to assign 3/3 Ile, 10/10 Val, and 42/44 Leu methyl groups. Data were collected on both fully $^{2}H/^{13}C/^{15}N/^{1}H(I^{\delta1}/L/V)$-labeled samples and on samples containing Leu and Val residues that were labeled $^{1}H/^{13}C$ on one methyl group and $^{2}H/^{12}C$ on the other methyl group.[39] All Gln NH_2 resonances were assigned using a two-dimensional version of the $H_2N(CO)CGCB$ sequence.[41] Phenylalanine resonances were assigned through analysis of NOE spectroscopy (NOESY), COSY, and TOCSY spectra. NMR data were processed using NMRPipe[42] and analyzed using NMRView.[43]

Restraint collection

Three-dimensional ^{15}N- and/or ^{13}C-edited NOESY–HSQC spectra[44] were collected in H_2O at 20 °C on $^{2}H/^{15}N$, $^{2}H/^{13}C/^{15}N$, $^{2}H/^{13}C/^{15}N/^{1}H(I^{\delta1}/L/V)$, and $^{2}H/^{13}C/^{15}N/^{1}H(I^{\delta1}/L/V)$ (^{15}N–F) samples in H_2O and D_2O at 20 °C with 200 ms and 300 ms mixing times. A three-dimensional, constant-time NOESY–HSQC was collected in D_2O with a 300-ms mixing time. Isotopic half-filtered NOESY spectra[45] were also collected on the $^{2}H/^{13}C/^{15}N/^{1}H(I^{\delta1}/L/V)$ (^{15}N–F)-labeled sample in H_2O. Backbone ^{15}N relaxation data were collected using standard two-dimensional sensitivity-enhanced experiments. R_1 data were collected with 0.12, 0.24 (×2), 0.64, 1.28, and 2.56 s relaxation delays; R_2 data were collected with 0.017, 0.025 (×2), 0.034, 0.051, and 0.076 s relaxation delays; heteronuclear NOE data were collected using a 6-s recycle delay with 3-s proton saturation applied by a train of 120° pulses separated by 5-ms delays. Data were analyzed using Modelfree 4.20[46,47] with the FAST-Modelfree scripts.[48]

$^{1}D_{HN}$ were obtained using in-phase/anti-phase HSQC or transverse relaxation optimized spectroscopy–HNCO sequences[49,50] applied to isotropic protein samples or those embedded in acrylamide gels.[51–54] Uncharged polyacrylamide gels (7% acrylamide, 19:1 acrylamide:bis-acrylamide; Sigma) were polymerized overnight in a 6-mm-diameter gel funnel (New Era Enterprises, Vineland, NJ), extensively dialyzed, and dried at room temperature. The dried gel was reconstituted in the 6-mm funnel by addition of 400 μl of NOXO1β PX (0.5 mM concentration in NMR buffer) and overnight hydration. Fully hydrated gels were inserted into a 5-mm NMR tube using the 6.0- to 4.2-mm funnel. Charged gels were prepared at 7% acrylamide with 25% 3-(acrylamidopropyl)-trimethylammonium chloride. Gels were polymerized inside of a piece of 1/8″ (i.d.) Tygon tubing, dialyzed extensively against water, and dried at room temperature for ~2 days on a sheet of Teflon. The dried gel was placed into a 5-mm Shigemi tube and hydrated overnight with 300 μl of 0.5 mM NOXO1β PX in NMR buffer. The gel was longitudinally compressed to 90% of its original length using the Shigemi plunger. Initial estimates of Da and Rh were estimated from the distribution of $^{1}D_{HN}$[55] and from calculations using homology models of NOXO1β based on $p47^{phox}$.[56] These values were refined at the Xplor-NIH water refinement stage and used iteratively in ARIA calculations.

Structure calculation

Initial structures were calculated using ARIA2.2/CNS 1.2,[57,58] which produced unambiguous and ambiguous assignment tables. These restraints were used for *de novo* structure calculation using Xplor-NIH 2.26. Xplor was used for final structure calculations to facilitate incorporation of ^{1}H chemical shift and RDC restraints and to simplify execution of the explicit water refinement. We calculated 32 structures *in vacuo* without electrostatics, and we then refined the 14 low-energy structures in explicit water with the electrostatic potential turned on. Restraints involving Phe side chains were set at 1.8 Å for the lower limit and either 4.0 or 6.0 Å for the upper limit, depending on cross-peak intensity. All other restraints were automatically calibrated by ARIA. For water refinement, the restraints were rescaled and binned based on internal distance standards using a total range of 1.8–5, 1.8–6, or 1.8–7 Å depending on type of experiment and mixing time (e.g., the upper bounds for distances between methyl protons measured by the 300-ms NOESY was set to 7 Å). Xplor calculations used the initial unambiguous and ambiguous distance restraints, 55 χ_1 (confidence ≥ 0.7)[59] and 222 backbone $\phi\,\psi$[60,61] dihedral angle restraints, 53 ^{1}H methyl chemical shifts, 92 $^{1}H^{N}$–^{15}N residual dipolar coupling restraints obtained from axially compressed acrylamide gels,[51,52] and 64 ^{1}H–^{15}N residual dipolar couplings obtained from charged acrylamide gels.[53,54] The hydrogen bond restraint list was built iteratively based on the presence of secondary structural elements identified from backbone dihedral angles, cross-strand H^{N}–H^{N} NOEs, and analysis of structures using HB-PLUS.[62] Ultimately, we incorporated 63 hydrogen bond restraints. Water refinement was carried out using Xplor-NIH 2.26 with protocols developed by Nabuurs *et al.* and Linge *et al.*[63,64] Structural statistics for 14 low-energy structures are shown in Table 1. Structure figures were prepared using PyMOL[65] and CorelDraw.

SPR experiments

Liposomes were prepared as previously described.[66] Briefly, target lipids including 1-palmitoyl-2-oleoyl-*sn*-glycero-3-phosphatidic acid, 1-palmitoyl-2-oleoyl-*sn*-glycero-3-phosphatidylserine, or dipalmitoyl PtdIns phosphates were dissolved in $CHCl_3/CH_3OH/H_2O$ (1:2:0.8) and added to 1-palmitoyl-2-oleoyl-*sn*-glycero-3-phosphatidylcholine or 1-palmitoyl-2-oleoyl-*sn*-glycero-3-phosphatidylethanolamine in $CHCl_3$ at a 1-palmitoyl-2-oleoyl-*sn*-glycero-3-phosphatidylcholine:1-palmitoyl-2-oleoyl-*sn*-glycero-3-phosphatidylethanolamine:target lipid ratio of 74:20:6. The mixture was dried first under N_2 and then under vacuum to remove residual $CHCl_3$, hydrated in SPR buffer, and extruded 19 times with a LiposoFast extruder (Avestin, Ottawa, ON) through two stacked polycarbonate membranes (0.1 μm pore size). Dipalmitoyl PtdIns phosphates were purchased from Cell Signals, Kinnear, OH; all other lipids were purchased from Avanti Polar Lipids, Alabaster, AL.

SPR data were collected at 25 °C on a Biacore T100. Liposomes (0.1 mM total lipid concentration) were immobilized on an L1 chip by flowing over the surface at 5 μl/min for 600 s. Typical lipid loading was

~6000 RU/lane. This value suggests that the lipids are forming a contiguous bilayer on the chip surface, rather than remaining as intact liposomes,[67] and minimizes nonspecific protein binding to the L1 chip surface without introducing mass transfer effects.[24,29] The bilayer was washed with three 6-μl injections of 50 mM NaOH at 100 μl/min interspersed with SPR buffer and blocked with a 25-μl injection of 0.1 mg/ml fatty-acid-free bovine serum albumin at 5 μl/min. Following the wash steps, SPR buffer was flowed across reference and target lanes at 5 μl/min for 48 s. Protein solutions at 0, 0.05, 0.1, 0.5, 1.0, 5.0, and 10.0 μM NOXO1β PX or $p40^{phox}$ PX (control) were injected at 5 μl/min, and data were collected for 1200 s, followed by regeneration of the chip surface by washing with 40 mM 3-[(3-cholamidopropyl)dimethylammonio]propanesulfonic acid (Anatrace, Maumee, OH) and 40 mM *n*-octyl-β-D-glucopyranoside (Anatrace). Three independent sensorgrams were collected for each lipid and protein concentration tested.

SPR analysis

Because we observed high levels of binding to the background PE/PC lipids in the reference lane (broken line, Fig. 4a and b), we have used the ratios, rather than the differences, between baseline-subtracted target lipid *versus* reference lane responses to assess relative binding by the NOXO1β PX domain to different phospholipids (as suggested by Eric Roush, Biacore Application Scientist). This minimizes errors derived from between-run differences in initial lipid loading. Specifically, we use the mean RU value of 40 s prior to protein injection as a baseline and subtract this from the response curve after protein injection. The target:reference ratio is calculated as the mean of the ratios of the baseline-subtracted target and reference RU between 160 and 560 s after protein injection (Supplemental Figure 2). The 160-s delay allows for stabilization of protein binding to the target and reference lanes. The standard deviation for a given target:reference ratio is ~0.01 over the 400-s averaging period. SPR binding data at 5 μM and 10 μM protein concentrations were analyzed in SigmaPlot v11 (Systat) using the Kruskal–Wallis one-way ANOVA on ranks ($p=0.005$ at 5 μM; $p=0.003$ at 10 μM) with subsequent application of Dunn's post-hoc test for unequal variances with $p=0.05$ as the criteria for significance.

Accession numbers

Resonance assignments have been deposited at BioMagResBank under accession code 16749. Structures and related data have been deposited at Research Collaboratory for Structural Bioinformatics under accession code 2L73.

Acknowledgements

This work is funded by National Institutes of Health grants R01AI064609 to D.A.H. and R01AI022564 to L.C.M. D.A.H thanks Pascal Mercier (Chenomx) and Charles Schwieters (National Institutes of Health) for Xplor/water refinement scripts. D.A.H. and N.Y.D. also thank Roy Hantgan (Wake Forest School of Medicine) and Eric Roush (Biacore) for advice and comments regarding SPR experiments.

Supplementary Data

Supplementary data associated with this article can be found, in the online version, at doi:10.1016/j.jmb.2012.01.058

References

1. Kim, Y. S., Morgan, M. J., Choksi, S. & Liu, Z. G. (2007). TNF-induced activation of the Nox1 NADPH oxidase and its role in the induction of necrotic cell death. *Mol. Cell*, **26**, 675–687.
2. Komatsu, D., Kato, M., Nakayama, J., Miyagawa, S. & Kamata, T. (2008). NADPH oxidase 1 plays a critical mediating role in oncogenic Ras-induced vascular endothelial growth factor expression. *Oncogene*, **27**, 4724–4732.
3. Shinohara, M., Adachi, Y., Mitsushita, J., Kuwabara, M., Nagasawa, A., Harada, S. *et al.* (2010). Reactive oxygen generated by NADPH oxidase 1 (Nox1) contributes to cell invasion by regulating matrix metalloprotease-9 production and cell migration. *J. Biol. Chem.* **285**, 4481–4488.
4. Bedard, K. & Krause, K. H. (2007). The NOX family of ROS-generating NADPH oxidases: physiology and pathophysiology. *Physiol. Rev.* **87**, 245–313.
5. Dutta, S. & Rittinger, K. (2010). Regulation of NOXO1 activity through reversible interactions with p22 and NOXA1. *PLoS One*, **5**, e10478.
6. Cheng, G. & Lambeth, J. D. (2005). Alternative mRNA splice forms of *NOXO1*: differential tissue expression and regulation of Nox1 and Nox3. *Gene*, **356**, 118–126.
7. Bravo, J., Karathanassis, D., Pacold, C. M., Pacold, M. E., Ellson, C. D., Anderson, K. E. *et al.* (2001). The crystal structure of the PX domain from $p40^{phox}$ bound to phosphatidylinositol 3-phosphate. *Mol. Cell*, **8**, 829–839.
8. Zhou, C. Z., de LaSierra-Gallay, I. L., Quevillon-Cheruel, S., Collinet, B., Minard, P., Blondeau, K. *et al.* (2003). Crystal structure of the yeast Phox homology (PX) domain protein Grd19p complexed to phosphatidylinositol-3-phosphate. *J. Biol. Chem.* **278**, 50371–50376.
9. Cheng, G. & Lambeth, J. D. (2004). NOXO1, regulation of lipid binding, localization, and activation of Nox1 by the phox homology (PX) domain. *J. Biol. Chem.* **279**, 4737–4742.
10. Takeya, R., Taura, M., Yamasaki, T., Naito, S. & Sumimoto, H. (2006). Expression and function of Noxo1γ, an alternative splicing form of the NADPH oxidase organizer 1. *FEBS J.* **273**, 3663–3677.
11. Ueyama, T., Lekstrom, K., Tsujibe, S., Saito, N. & Leto, T. L. (2007). Subcellular localization and function of

alternatively spliced Noxo1 isoforms. *Free Radical Biol. Med.* **42**, 180–190.
12. Banfi, B., Clark, R. A., Steger, K. & Krause, K. H. (2003). Two novel proteins activate superoxide generation by the NADPH oxidase NOX1. *J. Biol. Chem.* **278**, 3510–3513.
13. Kanai, F., Liu, H., Field, S. J., Akbary, H., Matsuo, T., Brown, G. E. *et al.* (2001). The PX domains of p47phox and p40phox bind to lipid products of PI(3)K. *Nat. Cell Biol.* **3**, 675–678.
14. Geiszt, M., Lekstrom, K., Witta, J. & Leto, T. L. (2003). Proteins homologous to $p47^{phox}$ and $p67^{phox}$ support superoxide production by NAD(P)H oxidase 1 in colon epithelial cells. *J. Biol. Chem.* **278**, 20006–20012.
15. Takeya, R., Ueno, N., Kami, K., Taura, M., Kohjima, M., Izaki, T. *et al.* (2003). Novel human homologues of $p47^{phox}$ and $p67^{phox}$ participate in activation of superoxide-producing NADPH oxidases. *J. Biol. Chem.* **278**, 25234–25246.
16. Hiroaki, H., Ago, T., Ito, T., Sumimoto, H. & Kohda, D. (2001). Solution structure of the PX domain, a target of the SH3 domain. *Nat. Struct. Biol.* **8**, 526–530.
17. Xu, J., Liu, D., Gill, G. & Songyang, Z. (2001). Regulation of cytokine-independent survival kinase (CISK) by the Phox homology domain and phosphoinositides. *J. Cell Biol.* **154**, 699–705.
18. Xing, Y., Liu, D., Zhang, R., Joachimiak, A., Songyang, Z. & Xu, W. (2004). Structural basis of membrane targeting by the phox homology domain of cytokine-independent survival kinase (CISK-PX). *J. Biol. Chem.* **279**, 30662–30669.
19. Virbasius, J. V., Song, X., Pomerleau, D. P., Zhan, Y., Zhou, G. W. & Czech, M. P. (2001). Activation of the Akt-related cytokine-independent survival kinase requires interaction of its phox domain with endosomal phosphatidylinositol 3-phosphate. *Proc. Natl Acad. Sci. USA*, **98**, 12908–12913.
20. Parkinson, G. N., Vines, D., Driscoll, P. C. & Djordjevic, S. (2008). Crystal structures of PI3K-C2α PX domain indicate conformational change associated with ligand binding. *BMC Struct. Biol.* **8**, 13.
21. Stahelin, R. V., Karathanassis, D., Bruzik, K. S., Waterfield, M. D., Bravo, J., Williams, R. L. & Cho, W. (2006). Structural and membrane binding analysis of the phox homology domain of phosphoinositide 3-kinase-C2α. *J. Biol. Chem.* **281**, 39396–39406.
22. Wahl, M., Delbrueck, H., Oschkinat, H. & Heinemann, U. (2003). PDB entry 1KQ6; p47phox PX domain.
23. Karathanassis, D., Stahelin, R. V., Bravo, J., Perisic, O., Pacold, C. M., Cho, W. & Williams, R. L. (2002). Binding of the PX domain of $p47^{Phox}$ to phosphatidylinositol 3,4-biphosphate and phosphatidic acid is masked by an intramolecular interaction. *EMBO J.* **21**, 5057–5068.
24. Stahelin, R. V., Karathanassis, D., Murray, D., Williams, R. L. & Cho, W. (2007). Structural and membrane binding analysis of the phox homology domain of Bem1p. *J. Biol. Chem.* **282**, 25737–25747.
25. Noack, D., Rae, J., Cross, A. R., Ellis, B. A., Newburger, P. E., Curnutte, J. T. & Heyworth, P. G. (2001). Autosomal recessive chronic granulomatous disease caused by defects in *NCF-1*, the gene encoding the phagocyte p47-*phox*: mutations not arising in the *NCI-1* pseudogenes. *Blood*, **97**, 305–311.
26. Heyworth, P. G. & Cross, A. R. (2002). Chronic granulomatous disease mutations and the PX domain. *Nat. Cell Biol.* **4**, E110.
27. Song, X., Xu, W., Zhang, A., Huang, G., Liang, X., Virbasius, J. V. *et al.* (2001). Phox homology domains specifically bind phosphatidylinositol phosphates. *Biochemistry*, **40**, 8940–8944.
28. Zhan, Y., Virbasius, J. V., Song, X., Pomerleau, D. P. & Zhou, G. W. (2002). The $p40^{phox}$ and $p47^{phox}$ PX domains of NADPH oxidase target cell membranes via direct and indirect recruitment by phosphoinositides. *J. Biol. Chem.* **277**, 4512–4518.
29. Narayan, K. & Lemmon, M. A. (2006). Determining selectivity of phosphoinositide-binding domains. *Methods*, **39**, 122–133.
30. Vanhaesebroeck, B., Leevers, S. J., Ahmadi, K., Timms, J., Katso, R., Driscoll, P. C. *et al.* (2001). Synthesis and function of 3-phosphorylated inositol lipids. *Annu. Rev. Biochem.* **70**, 535–602.
31. Behnia, R. & Munro, S. (2005). Organelle identity and the signposts for membrane traffic. *Nature*, **438**, 597–604.
32. Di Paolo, G. & De Camilli, P. (2006). Phosphoinositides in cell regulation and membrane dynamics. *Nature*, **443**, 651–657.
33. Stahelin, R. V., Ananthanarayanan, B., Blatner, N. R., Singh, S., Bruzik, K. S., Murray, D. & Cho, W. (2004). Mechanism of membrane binding of the phospholipase D1 PX domain. *J. Biol. Chem.* **279**, 54918–54926.
34. Brown, D. I. & Griendling, K. K. (2009). Nox proteins in signal transduction. *Free Radical Biol. Med.* **47**, 1239–1253.
35. Sadok, A., Pierres, A., Dahan, L., Prevot, C., Lehmann, M. & Kovacic, H. (2009). NADPH oxidase 1 controls the persistence of directed cell migration by a Rho-dependent switch of α2/α3 integrins. *Mol. Cell. Biol.* **29**, 3915–3928.
36. Shinohara, M., Shang, W. H., Kubodera, M., Harada, S., Mitsushita, J., Kato, M. *et al.* (2007). Nox1 redox signaling mediates oncogenic Ras-induced disruption of stress fibers and focal adhesions by down-regulating Rho. *J. Biol. Chem.* **282**, 17640–17648.
37. Saarikangas, J., Zhao, H. & Lappalainen, P. (2010). Regulation of the actin cytoskeleton-plasma membrane interplay by phosphoinositides. *Physiol. Rev.* **90**, 259–289.
38. Davis, N. Y., McPhail, L. C. & Horita, D. A. (2011). Backbone ^{1}H, ^{15}N, and ^{13}C resonance assignments for the NOXO1β PX domain. *Biomol. NMR Assign.* **5**, 139–141.
39. Tugarinov, V. & Kay, L. E. (2003). Ile, Leu, and Val methyl assignments of the 723-residue malate synthase G using a new labeling strategy and novel NMR methods. *J. Am. Chem. Soc.* **125**, 13868–13878.
40. Link, Y. & Wagner, G. (1999). Efficient side-chain and backbone assignment in large proteins: application to tGCN5. *J. Biomol. NMR*, **15**, 227–239.
41. Farmer, B. T., II & Venters, R. A. (1996). Assignment of aliphatic side-chain $^{1}HN/^{15}N$ resonances in perdeuterated proteins. *J. Biomol. NMR*, **7**, 59–71.
42. Delaglio, F., Grzesiek, S., Vuister, G. W., Zhu, G., Pfeifer, J. & Bax, A. (1995). NMRPipe: a multidimensional spectral processing system based on UNIX pipes. *J. Biomol. NMR*, **6**, 277–293.

43. Johnson, B. A. & Blevins, R. A. (1994). NMRView: a computer program for the visualization and analysis of NMR data. *J. Biomol. NMR*, **4**, 603–614.
44. Xia, Y., Yee, A., Arrowsmith, C. H. & Gao, X. (2003). $^{1}H_{C}$ and $^{1}H_{N}$ total NOE correlations in a single 3D NMR experiment. ^{15}N and ^{13}C time-sharing in t_1 and t_2 dimensions for simultaneous data acquisition. *J. Biomol. NMR*, **27**, 193–203.
45. Otting, G. & Wüthrich, K. (1989). Extended heteronuclear editing of 2D ^{1}H NMR spectra of isotope-labeled proteins, using the $X(\omega_1, \omega_2)$ double half filter. *J. Magn. Reson.* **85**, 586–594.
46. Mandel, A. M., Akke, M. & Palmer, A. G., III (1995). Backbone dynamics of *Escherichia coli* ribonuclease HI: correlations with structure and function in an active enzyme. *J. Mol. Biol.* **246**, 144–163.
47. Palmer, A. G., III, Rance, M. & Wright, P. E. (1991). Intramolecular motions of a zinc finger DNA-binding domain from Xfin characterized by proton-detected natural abundance ^{13}C heteronuclear NMR spectroscopy. *J. Am. Chem. Soc.* **113**, 4371–4380.
48. Cole, R. & Loria, J. P. (2003). FAST-Modelfree: a program for rapid automated analysis of solution NMR spin-relaxation data. *J. Biomol. NMR*, **26**, 203–213.
49. Yang, D., Venters, R. A., Mueller, G. A., Choy, W. Y. & Kay, L. E. (1999). TROSY-based HNCO pulse sequences for the measurement of $^{1}HN–^{15}N$, $^{15}N–^{13}CO$, $^{1}HN–^{13}CO$, $^{13}CO–^{13}C^{\alpha}$ and $^{1}HN–^{13}C^{\alpha}$ dipolar couplings in ^{15}N, ^{13}C, ^{2}H-labeled proteins. *J. Biomol. NMR*, **14**, 333–343.
50. Ottiger, M., Delaglio, F. & Bax, A. (1998). Measurement of *J* and dipolar couplings from simplified two-dimensional NMR spectra. *J. Magn. Reson.* **131**, 373–378.
51. Chou, J. J., Gaemers, S., Howder, B., Louis, J. M. & Bax, A. (2001). A simple apparatus for generating stretched polyacrylamide gels, yielding uniform alignment of proteins and detergent micelles. *J. Biomol. NMR*, **21**, 377–382.
52. Tycko, R., Blanco, F. J. & Ishii, Y. (2000). Alignment of biopolymers in strained gels: a new way to create detectable dipole–dipole couplings in high-resolution biomolecular NMR. *J. Am. Chem. Soc.* **122**, 9340–9341.
53. Cierpicki, T. & Bushweller, J. H. (2004). Charged gels as orienting media for measurement of residual dipolar couplings in soluble and integral membrane proteins. *J. Am. Chem. Soc.* **126**, 16259–16266.
54. Meier, S., Häussinger, D. & Grzesiek, S. (2002). Charged acrylamide copolymer gels as media for weak alignment. *J. Biomol. NMR*, **24**, 351–356.
55. Clore, G. M., Gronenborn, A. M. & Tjandra, N. (1998). Direct structure refinement against residual dipolar couplings in the presence of rhombicity of unknown magnitude. *J. Magn. Reson.* **131**, 159–162.
56. Schwieters, C. D., Kuszewski, J. J., Tjandra, N. & Clore, G. M. (2003). The Xplor-NIH NMR molecular structure determination package. *J. Magn. Reson.* **160**, 65–73.
57. Brünger, A. T., Adams, P. D., Clore, G. M., DeLano, W. L., Gros, P., Grosse-Kunstleve, R. W. *et al.* (1998). Crystallography & NMR system: a new software suite for macromolecular structure determination. *Acta Crystallogr., Sect. D: Biol. Crystallogr.* **54**, 905–921.
58. Rieping, W., Habeck, M., Bardiaux, B., Bernard, A., Malliavin, T. E. & Nilges, M. (2007). ARIA2: automated NOE assignment and data integration in NMR structure calculation. *Bioinformatics*, **23**, 381–382.
59. Berjanskii, M. V., Neal, S. & Wishart, D. S. (2006). PREDITOR: a web server for predicting protein torsion angle restraints. *Nucleic Acids Res.* **34**, W63–W69.
60. Shen, Y., Delaglio, F., Cornilescu, G. & Bax, A. (2009). TALOS: a hybrid method for predicting protein backbone torsion angles from NMR chemical shifts. *J. Biomol. NMR*, **44**, 213–223.
61. Cornilescu, G., Delaglio, F. & Bax, A. (1999). Protein backbone angle restraints from searching a database for chemical shift and sequence homology. *J. Biomol. NMR*, **13**, 289–302.
62. McDonald, I. K. & Thornton, J. M. (1994). Satisfying hydrogen bonding potential in proteins. *J. Mol. Biol.* **238**, 777–793.
63. Nabuurs, S. B., Nederveen, A. J., Vranken, W., Doreleijers, J. F., Bonvin, A. M., Vuister, G. W. *et al.* (2004). DRESS: a database of REfined solution NMR structures. *Proteins*, **55**, 483–486.
64. Linge, J. P., Williams, M. A., Spronk, C. A., Bonvin, A. M. & Nilges, M. (2003). Refinement of protein structures in explicit solvent. *Proteins*, **50**, 496–506.
65. DeLano, W. L. (2008). *The PyMOL Molecular Graphics System.* DeLano Scientific, LLC, Palo Alto, CA.
66. Shen, K., Sergeant, S., Hantgan, R. R., McPhail, L. C. & Horita, D. A. (2008). Mutations in the PX–$SH3_A$ linker of $p47^{phox}$ decouple $PI(3,4)P_2$ binding from NADPH oxidase activation. *Biochemistry*, **47**, 8855–8865.
67. Erb, E. M., Chen, X., Allen, S., Roberts, C. J., Tendler, S. J., Davies, M. C. & Forsen, S. (2000). Characterization of the surfaces generated by liposome binding to the modified dextran matrix of a surface plasmon resonance sensor chip. *Anal. Biochem.* **280**, 29–35.